# Insight into Benzothiadiazole Acceptor in D−A−π−A Configuration on Photovoltaic Performances of Dye-Sensitized Solar Cells

Haibo Zhu,[†] Wenqin Li,[†,‡] Yongzhen Wu,[†] Bo Liu,[§] Shiqin Zhu,[†] Xin Li,[∥] Hans Ågren,[∥] and Weihong Zhu*,[†]

[†]Shanghai Key Laboratory of Functional Materials Chemistry, Key Laboratory for Advanced Materials and Institute of Fine Chemicals, East China University of Science and Technology, Shanghai 200237, P. R. China

[‡]School of Urban Development and Environmental Engineering, Shanghai Second Polytechnic University, Shanghai 201209, P. R. China

[§]College of Chemistry and Material Science, Hebei Normal University, No. 20, East Road of Nan Er Huan, Shijiazhuang 050023, P. R. China

[∥]Division of Theoretical Chemistry and Biology, School of Biotechnology, KTH Royal Institute of Technology, SE-10691 Stockholm, Sweden

ABSTRACT: The option of conjugated π-linkers is critical for molecular engineering toward the energy-level strategy of donor−π−acceptor (D−π−A) sensitizers. There is always a balance in the optimization of a π-linker. The π-conjugation should be enlarged to expand the light-harvesting capability of sensitizers for an increase in photocurrent; however, the oversized π-linker also would affect seriously the photovoltage and photostability. Two sensitizers, **WS-22** and **WS-23**, are constructed without or with benzothiadiazole (BTD) in a molecular skeleton, aiming to gain insight into the effect of an auxiliary acceptor in D−A−π−A sensitizers on the photo-

physical and photovoltaic performances, especially focusing on the exploitation of the short circuit current density (J_{sc}) and open circuit voltage (V_{oc}). Compared with the typical D−π−A sensitizer **WS-22**, the incorporation of an auxiliary acceptor of BTD in **WS-23** can improve the light-harvesting ability both in red-shifting the absorption peaks and the increment of absorption coefficient. The predominant increase by 15.6% in light-harvesting efficiency (LHE) of **WS-23** results in a relatively higher J_{sc} from 13.77 (**WS-22**) to 16.91 mA cm^{-2} (**WS-23**). Moreover, the improvement of the V_{oc} in **WS-23** is originated by a synergy contribution of the uplifting of E_{CB} and inhibition of charge recombination. The stepped light-induced transient (SLIT) measurements indicate that the introduction of BTD can negatively shift the conduction band of the TiO$_2$ film. For **WS-23**, the higher molecular dipole moment can bring forth a more effective charge separation between donor and acceptor units, also resulting in an increase in V_{oc}. The incorporated BTD unit can increase V_{oc} by 57 mV, arising from the CB edge shift of TiO$_2$ (accounting for 40%, 23 mV) and the retarding charge recombination (accounting for 60%, 34 mV). As a consequence, **WS-23** realizes an optimizing photovoltaic efficiency (η = 8.15%), with an improvement of 36.5% with respect to **WS-22**.

KEYWORDS: *Organic sensitizers, Benzothiadiazole, Auxiliary acceptor, Solar cells, Photovoltaic performances*
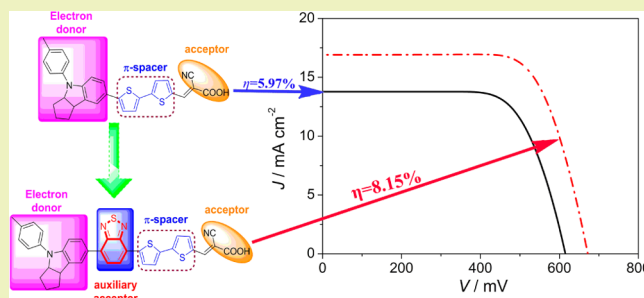
INTRODUCTION

Dye-sensitized solar cells (DSSCs) have attracted worldwide attention as a potential alternative of continuous energy supply devices because of their high performance, easy fabrication, and low-cost.[1,2] A typical DSSC is composed of a dye-anchored mesoporous semiconductor film as the anode electrode, a Pt counter electrode, and electrolyte.[3] As a key component in DSSCs, the photosensitizer absorbs the sunlight to inject the excited electron into the semiconductor conduction band. A workable dye should be energy-matched with the semiconductor materials and redox species used in the electrolyte. Besides, good light-harvesting ability as well as photo- and chemical-stability is necessary for an efficient sensitizer. During the past two decades, thousands of organic sensitizers have

been developed with the D−π−A configuration, exhibiting a promising photo-to-electricity conversion efficiency.[4−8] As is well known, the π-linker segment has influences on the photophysical and electrochemical properties to a large extent, which also greatly affects the photovoltaic performance of sensitizers.[9,10] Actually, there is a balance in the optimization of π-linker. One should enlarge the π-conjugation to expand the light-harvesting capability of the sensitizer for an increase in photocurrent; however, the oversized π-linker also would affect seriously the photovoltage and photostability of DSSCs.

Our group has developed a series of D−π−A sensitizers bearing indoline as the electron-donating group, a promising electron donor with priority in optimizing the absorption spectra of sensitizers.[11,12] However, such indoline-based D−π−A sensitizers show limitation in photostability, which restricts their practicable application.[4] To overcome the problem, a D−A−π−A configuration was proposed with an auxiliary acceptor between the donor and conjugation bridge.[13−17] The D−A−π−A configuration can significantly reduce the HOMO−LUMO energy gap along with an improved light stability, highly desirable in photovoltatic optimization of sensitizers. However, a systematical comparison with or without additional auxiliary acceptors in the skeleton of sensitizers has rarely been studied.[18−21] Dithiophene is a common segment or building block of low-band gap semiconducting polymers in bulk heterojunction (BHJ) organic solar cells and light-emitting diodes, favorable in extension of π-conjugation.[22] Herein, we specifically introduce the dithiophene unit into **WS-22** and **WS-23** (Figure 1) as a π-spacer. Meanwhile, a benzothiadiazole
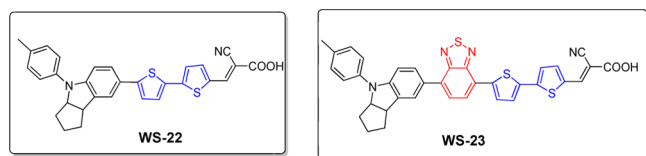

Figure 1. Chemical structures of sensitizers **WS-22** and **WS-23**.

(BTD) moiety is incorporated as an additional electron-withdrawing group located between the indoline donor and dithiophene bridge to systematically investigate the effect of BTD on photophysical and photovoltaic performances. Given BTD as an auxiliary acceptor, **WS-23** exhibits an overall conversion efficiency of 8.15%, an obvious enhancement of 36.5% with respect to **WS-22**. As demonstrated, the incorporation of BTD in **WS-23** is beneficial to the efficient light-harvesting and electron injection process, thus generating relatively high photocurrent. Both the stepped light-induced transient (SLIT) and theory calculations indicate that **WS-23**-based solar cells show a higher conduction band (E_{CB}) and slower charge recombination. As a consequence, the D−A−π−A-featured sensitizers are promising candidates for highly efficient DSSCs.

■ EXPERIMENTAL SECTION

Materials. The FTO-conducting glass (fluorine-doped SnO_2, sheet resistance 7 Ω/square, transmission 90% in the visible region) was obtained from Touki Co. TiO_2 paste (PST-18NR for 20 nm and PST-400C for 400 nm) was provided by JGC C&C, Ltd. 5-Bromo-5′-formyl-2,2′-bithiophene (2), bis(pinacolato)diboron, $Pd(PPh_3)_4$, and n-butyllithium in hexane were purchased from J&K Scientific, Ltd. All other regents and solvents were purchased as analytical grade from Sinopharm Chemical Reagent Co., Ltd.

Characterization. ^1H and ^{13}C NMR spectra were recorded on a Bruker AM 400 spectrometer with tetramethylsilane (TMS) as the internal standard, operating at 400 and 100 MHz, respectively. High-resolution mass spectrometry (HRMS) was performed using a Waters LCT Premier XE spectrometer. The UV−vis spectra were recorded with a Varian Cary 100 spectrophotometer. Cyclic voltammograms were performed with a Versastat II electrochemical workstation (Princeton Applied Research) using a normal three-electrode cell with a Pt working electrode, Pt wire counter electrode, and regular calomel reference electrode in a saturated KCl solution. An amount of 0.1 M tetrabutylammonium hexafluorophosphate ($TBAPF_6$) was used as the supporting electrolyte in CH_2Cl_2.

Theory Calculation. Density functional theory (DFT) and time-dependent (TD)-DFT calculations were performed to find out the origination of the absorption bands. Here, DFT calculations solve the time-independent Schrödinger equation, which describes the stationary states. In particular, DFT can be employed to optimize the ground state geometry and to gain insight into the electronic structure of the molecule or cluster of interest. It is a very widely used first-principles approach for modeling ground-state properties. TD-DFT, which is an extension of DFT, solves the time-dependent Schrödinger equation for excited-state properties. Owing to its efficiency, TD-DFT becomes increasingly popular in the modeling of electronic excitations and charge transfer effects, and the accuracy of the result is quite satisfactory provided that proper functional and basis sets are used in the calculations. The ground-state geometries and frontier molecular orbitals were computed using the hybrid PBE0 functional[23,24] and the 6-311G(d,p) basis set.[25,26] Frequency analyses were conducted to confirm that the optimized geometries are true minima. At the optimized geometries, TD-DFT calculations were carried out using the range-separated CAM-B3LYP functional[27] and the 6-311+(2d,p) basis set. Solvent effects of CH_2Cl_2 were taken into account by the polarizable continuum model (PCM) in both geometry optimizations and TD-DFT calculations. All theoretical calculations were carried out using the Gaussian 09 program package.

Preparation and Fabrication of DSSCs. Eight micrometer nanocrystalline TiO_2 electrodes with a 4 μm scattering layer were prepared and modified following the reported procedure. The thickness of TiO_2 film was measured by a surface profiler (Dektak Co., Ltd., Model DAKTAK II). The dye-loaded electrodes were prepared by dipping TiO_2 electrodes (0.3 cm × 0.2 cm) into a 0.3 mM dye solution ($CHCl_3$/EtOH = 3/1) with coadsorbent deoxycholic acid (DCA, 15 mM) for 12 h. To prepare the counter electrode, the Pt catalyst was deposited on the cleaned FTO glass by coating with a drop of H_2PtCl_6 solution (50 mM in ethanol solution) with the heat treatment at 500 °C for 30 min. In this work, 0.6 M 1-butyl-3-methylimidiazolium iodide (BMII), 0.1 M LiI, 0.05 M I_2, and 0.6 M tert-butylpyridine (TBP) in acetonitrile were used as the redox electrolyte.

Photovoltaic Measurements. Photovoltaic measurements were measured under irradiation of an AM 1.5 solar simulator equipped with a 150 W xenon lamp (OTENTO-SUN II, Bunkoukeiki Co., Ltd.). The power of the simulated light was calibrated to 100 mW cm^{-2} using a standard reference silicon cell (BS-520, Bunkoukeiki Co., Ltd.). I−V curves were obtained by applying an external bias (scanning from 800 to −100 mV) to the cell and measuring the generated photocurrent with a Keithley model 2400 digital source meter. The voltage step and delay time of photocurrent were 1 mV and 20 ms, respectively. The photocurrent action spectra were measured with a monochromator (M10-T, Bunkoukeiki Co., Ltd.). The intensity of the monochromic light was calibrated by a reference silicon cell (S1337−1010BQ, Bunkoukeiki Co., Ltd.).

Measurement of Electron Lifetime and Electron Density. Electron lifetime and electron density in the complete DSSCs were measured by the stepped light-induced transient measurements of photocurrent and photovoltage using a DSSCs evaluation system PSL-100 (EKO Co. Ltd.). A laser (λ = 660 nm) was used as the light source. The transients were induced by a stepwise change in the laser intensity, which was controlled by adjusting its voltage. The photocurrent and photovoltage transients were monitored using a digital oscilloscope through an amplifier. By varying the laser intensity, the lifetime could be estimated over a range of open circuit voltages by fitting a decay of the photovoltage transient with $\exp(-t/\tau)$. The electron density measurement was performed as follows: The DSSCs were illuminated for 5 s, while a bias voltage was applied to make the cell be open circuited, and then the laser was shut down, while simultaneously, the cell was switched from open to short circuit. The resulting current was measured in 25 s, and then the electron density could be calculated through integrating the quantity of electric charge. All experiments were conducted at room temperature.

Synthesis of 3. To a solution of **1** (235 mg, 0.72 mmol) and dry THF (20 mL) was added n-BuLi in hexane (0.33 mL, 0.79 mmol)

dropwise at −78 °C under the protection of argon. The solution was stirred at the same temperature for 1 h, and $B(OCH_3)_3$ (90 mg, 0.87 mmol) was added. After stirring at the temperature for 4 h, the mixture was gradually warmed to room temperature and stirred overnight for the next Suzuki reaction without purification. The previous mixture was reacted with **2** (261 mg, 0.96 mmol) under Suzuki coupling reaction conditions using $Pd(PPh_3)_4$ (81 mg, 0.07 mmol) and a 2 M K_2CO_3 (15 mL) aqueous solution in THF (30 mL) solution at 80 °C for 10 h. After cooling to room temperature, water was added and extracted with CH_2Cl_2. The combined extracts were washed with brine and dried over anhydrous magnesium sulfate. The solvent was removed by rotary evaporation. The crude product was purified by column chromatography with petroleum ether/CH_2Cl_2 (2/1, v/v) as eluent on silica gel to afford **3** as a red solid (120 mg, 37.8%). ^{1}H NMR (400 MHz, CDCl$_3$, δ, ppm): 9.84 (s, 1 H), 7.66 (d, J = 4.0 Hz, 1 H), 7.35 (s, 1 H), 7.30 (d, J = 3.7 Hz, 1 H), 7.28 (d, J = 2.0 Hz, 1 H), 7.21 (d, J = 4.0 Hz, 1 H), 7.19−7.16 (m, 4 H), 7.11 (d, J = 3.9 Hz, 1 H), 6.86 (d, J = 8.3 Hz, 1 H), 4.83 (m, 1 H), 3.85 (m, 1 H), 2.34 (s, 3 H), 2.14−2.02 (m, 1 H), 1.97−1.87 (m, 2 H), 1.84−1.75 (m, 1 H), 1.73−1.69 (m, 1 H), 1.57−1.50 (m, 1 H). ^{13}C NMR (100 MHz, CDCl$_3$, δ, ppm): 182.41, 148.49, 147.99, 147.82, 140.79, 139.90, 137.64, 135.76, 132.56, 131.96, 129.86, 127.32, 125.50, 123.63, 123.30, 122.33, 121.78, 120.41, 107.43, 69.32, 45.26, 35.15, 33.65, 24.42, 20.84. HRMS−ESI (m/z): [M + H]$^+$ Calcd. for $C_{27}H_{24}NOS_2$, 442.1299; found, 442.1296.

Synthesis of WS-22. A mixture of **3** (102 mg, 0.23 mmol), cyanoacetic acid (157 mg, 1.85 mmol), and piperidine (0.5 mL) in acetonitrile was stirred and heated at 80 °C for 8 h under argon. The crude product was extracted with CH_2Cl_2, washed with water, and dried over anhydrous magnesium sulfate. The solvent was removed by rotary evaporation. The crude product was purified by column chromatography with CH_3OH/CH_2Cl_2 (1/10, v/v) as eluent on silica gel to afford **WS-22** as a deep red solid (92 mg, 78%). ^{1}H NMR (400 MHz, DMSO, δ, ppm): 8.22 (s, 1 H), 7.76 (d, J = 4.0 Hz, 1 H), 7.47 (s, 2 H), 7.45 (d, J = 4.0 Hz, 1 H), 7.35 (dd, J = 8.5, 2.7 Hz, 2 H), 7.25−7.14 (m, 4 H), 6.83 (d, J = 8.3 Hz, 1 H), 4.87 (m, 1 H), 3.83 (m, 1 H), 2.28 (s, 3 H), 2.14−1.97 (m, 1 H), 1.87−1.67 (m, 3 H), 1.67−1.56 (m, 1 H), 1.44−1.31 (m, 1 H). ^{13}C NMR (100 MHz, DMSO, δ, ppm): 163.64, 147.54, 145.96, 139.31, 135.68, 134.43, 131.86, 131.00, 129.78, 127.35, 125.15, 123.81, 123.06, 122.48, 121.94, 119.76, 106.85, 68.29, 44.43, 34.77, 33.03, 23.94, 20.37. HRMS−ESI (m/z): [M − H]$^-$ Calcd. for $C_{30}H_{23}N_2O_2S_2$, 507.1201; found, 507.1200.

Synthesis of 5. A mixture of **4** (392 mg, 0.85 mmol), bis(pinacolato)diboron (300 mg, 1.18 mmol), $Pd(PPh_3)_4$ (92 mg, 0.08 mmol), and potassium acetate (334 mg, 3.4 mmol) in fresh toluene (30 mL) was stirred and heated at 120 °C for 12 h under argon. After cooling to room temperature, the mixture was washed with water and dried over anhydrous magnesium sulfate. The solvent was removed by rotary evaporation. The crude product was purified by column chromatography with ethyl acetate/CH_2Cl_2 (1/2, v/v) as eluent on silica gel to afford **5** as a red solid (206 mg, 47.6%). ^{1}H NMR (400 MHz, CDCl$_3$, δ, ppm): 8.21 (d, J = 7.0 Hz, 1 H), 7.78 (s, 1 H), 7.73 (dd, J = 8.4, 1.9 Hz, 1H), 7.64 (d, J = 7.0 Hz, 1H), 7.23 (d, J = 8.4 Hz, 2 H), 7.17 (d, J = 8.4 Hz, 2 H), 7.01 (d, J = 8.3 Hz, 1 H), 4.85 (m, 1 H), 3.93 (m, 1 H), 2.34 (s, 3 H), 2.14−2.02 (m, 1 H), 1.99−1.85 (m, 3 H), 1.73−1.69 (m, 1 H), 1.62−1.53 (m, 1 H), 1.24 (s, 12 H). ^{13}C NMR (100 MHz, CDCl$_3$, δ, ppm): 158.43, 153.47, 148.75, 140.08, 139.50, 137.73, 135.31, 131.77, 129.81, 129.19, 127.15, 125.76, 125.21, 107.33, 84.18, 69.31, 45.40, 35.21, 33.70, 24.93, 24.86, 24.45, 20.83. HRMS−ESI (m/z): [M + H]$^+$ Calcd. for $C_{30}H_{33}{}^{11}BN_3O_2S$, 510.2387; found, 510.2383.

Synthesis of 6. Compound **5** (192 mg, 0.38 mmol), 5-bromo-5′-formyl-2, 2′-bithiophene (125 mg, 0.46 mmol), $Pd(PPh_3)_4$ (46 mg, 0.04 mmol), and K_2CO_3 (2 M, 15 mL) were dissolved in THF (40 mL), and the mixture was heated at 80 °C for 10 h under argon. After cooling to room temperature, the mixture was extracted with CH_2Cl_2. The combined organic layers were washed with brine and dried over anhydrous magnesium sulfate. The solvent was removed by rotary evaporation, and the residue was purified by column chromatography with petroleum ether/CH_2Cl_2 (2/1, v/v) as eluent on silica gel to

afford **6** as a red solid (112 mg, 51.1%). ^{1}H NMR (400 MHz, CDCl$_3$, δ, ppm): 9.89 (s, 1 H), 8.04 (d, J = 4.0 Hz, 1 H), 7.94 (d, J = 7.6 Hz, 1 H), 7.79 (s, 1 H), 7.74 (dd, J = 8.4, 2.0 Hz, 1 H), 7.71 (d, J = 3.9 Hz, 1 H), 7.69 (d, J = 7.6 Hz, 1 H), 7.46 (d, J = 3.9 Hz, 1 H), 7.37 (d, J = 3.9 Hz, 1 H), 7.25−7.16 (m, 4 H), 7.03 (d, J = 8.4 Hz, 1 H), 4.89 (m, 1H), 3.95 (m, 1 H), 2.35 (s, 3 H), 2.14−2.04 (m, 1 H), 2.02−1.91 (m, 2 H), 1.87−1.76 (m, 1 H), 1.73−1.59 (m, 2 H). ^{13}C NMR (100 MHz, CDCl$_3$, δ, ppm): 182.50, 154.03, 152.75, 148.71, 147.23, 141.66, 141.53, 140.01, 137.47, 136.41, 135.43, 134.34, 134.22, 131.87, 129.83, 128.96, 127.63, 126.91, 126.87, 126.33, 125.92, 125.55, 124.24, 123.68, 120.44, 107.93, 69.32, 45.41, 35.23, 33.69, 24.45, 20.83. HRMS−ESI (m/z): [M + H]$^+$ Calcd. for $C_{33}H_{26}N_3OS_3$, 576.1238; found, 576.1234.

Synthesis of WS-23. The synthetic process of **WS-23** is similar to **WS-22** (Scheme 1). ^{1}H NMR (400 MHz, DMSO, δ, ppm): 8.42 (s, 1

Scheme 1. Synthetic Routes of WS-22 and WS-23
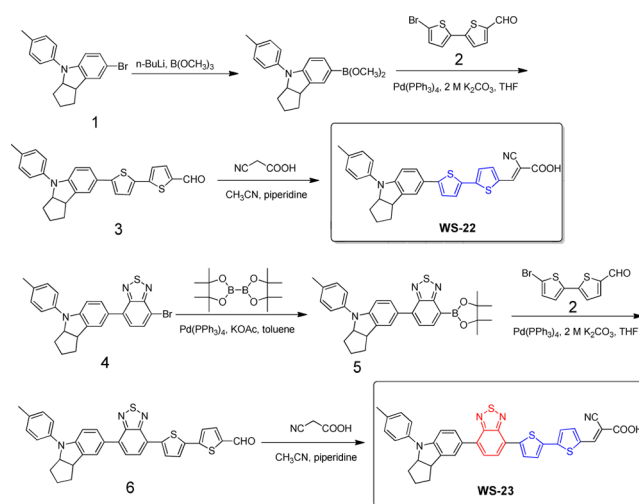
H), 8.09 (d, J = 7.7 Hz, 1 H), 8.05 (d, J = 4.1 Hz, 1 H), 7.92 (d, J = 4.1 Hz, 1 H), 7.82 (s, 1 H), 7.73 (d, J = 7.6 Hz, 2 H), 7.64 (d, J = 4.0 Hz, 1 H), 7.58 (d, J = 4.0 Hz, 1 H), 7.20 (q, J = 8.2 Hz, 4 H), 6.91 (d, J = 8.4 Hz, 1 H), 4.89 (m, 1 H), 3.86 (m, 1 H), 2.29 (s, 3 H), 2.11−1.95 (m, 1 H), 1.89−1.68 (m, 3 H), 1.67−1.55 (m, 1 H), 1.50−1.31 (m, 1 H). ^{13}C NMR (100 MHz, DMSO, δ, ppm): 163.58, 152.94, 151.81, 147.70, 140.92, 140.34, 139.41, 136.09, 135.06, 132.77, 130.94, 128.86, 127.73, 127.36, 126.32, 125.30, 124.91, 122.57, 119.73, 106.78, 68.34, 44.55, 34.88, 33.08, 23.96, 20.38. HRMS−ESI (m/z): [M + H]$^+$ Calcd. for $C_{36}H_{27}N_4O_2S_3$, 643.1296; found, 643.1295.

■ RESULTS AND DISCUSSION

Photovoltaic Performances. Figure 2a shows the action spectra of the incident photon current efficiency (IPCE) as a function of the light excitation wavelength for DSSCs based on **WS-22** and **WS-23**. The IPCE values exceed 50% in the range of 330−550 nm for the typical D−π−A sensitizer **WS-22**. By introducing BDT into the molecular skeleton, the IPCE action spectra of **WS-23** become broader and higher, with a significant increase in integral area under the curve compared to **WS-22**. The IPCE values for **WS-23** exceed 70% in the range of 410−550 nm with a maximum value of 76% at 470 nm, and the onset of IPCE for WS-23 is red-shifted to 830 nm.

Figure 2b shows the plots of the photocurrent density (J) as a function of voltage (V) for the two DSSCs based on the two sensitizers with irradiation of the simulated AM 1.5 G sunlight (100 mW cm^{-2}). The photovoltaic parameters are summarized in Table 1. The DSSCs based on **WS-22** produced a η of 5.97% (J_{sc} = 13.77 mA cm^{-2}, V_{oc} = 615 mV, FF = 0.705). For the **WS-**
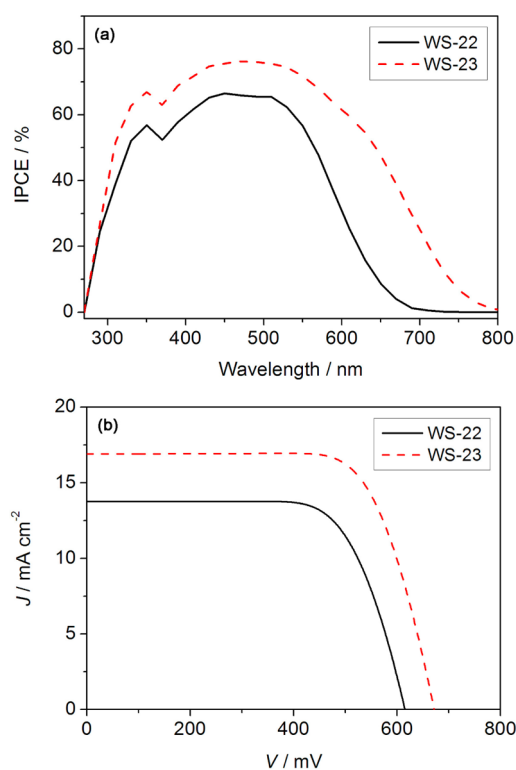
Figure 2. IPCE action spectra (a) and photocurrent voltage characteristics (b) for **WS-22**- and **WS-23**-based DSSCs.

Table 1. Optimized Photovoltaic Parameters of Dyes WS-22 and WS-23[a]

dyes	J_{sc} (mA cm^{-2})	V_{oc} (mV)	FF	η (%)
WS-22	13.77	615	0.705	5.97
WS-23	16.91	672	0.717	8.15

[a]The dye-loaded electrodes were prepared with optimized competition adsorption of coadsorbant (15 mM DCA).

23-based device, it yielded a higher J_{sc} and larger V_{oc} compared with **WS-22** and exhibited a higher η of 8.15% (J_{sc} = 16.91 mA cm^{-2}, V_{oc} = 672 mV, FF = 0.717). Compared with **WS-22**, the introduction of a BTD moiety in **WS-23** as an auxiliary moiety results in an improvement of 36.5% in overall conversion efficiency. Evidently, the additional acceptor group plays an important role in improving solar cell performance.

Effect on J_{sc}. The photocurrent of the DSSCs is associated with the absorption property, electron injection efficiency, and electron collection efficiency on the conduction glass (eq 1).

$$J_{sc} = \int IPCE\, d\lambda = \int LHE \times \Phi_{inj} \times \Phi_{col} \times d\lambda \quad (1)$$

where LHE is the light-harvesting efficiency of sensitizers, Φ_{inj} is electron injection efficiency from the excited sensitizers to the TiO$_2$ conduction band, and Φ_{col} is charge collection efficiency. Here Φ_{col} is determined by the structural morphology of the TiO$_2$ layer, which is almost the same process for the DSSC fabrication. To further shed light on the origination of the increment of photocurrent along with introduction of the BTD unit as the auxiliary acceptor, the aforementioned other factors (LHE and Φ_{inj}) are discussed below in detail.

In order to evaluate the driving force of the electron injection process for the two dyes, the electrochemical cyclic voltammetry measurement was carried out in CH$_2$Cl$_2$ (Figure

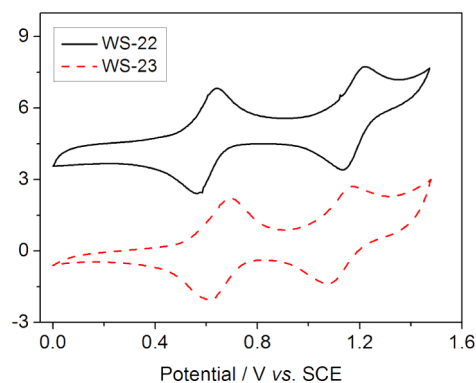3). Their corresponding HOMO orbitals can be calculated directly based on the first oxidation potential. The LUMO

Figure 3. Oxidative cyclic voltammetry plots of **WS-22** and **WS-23** measured in CH$_2$Cl$_2$.

orbital can be estimated through the equation of LUMO = HOMO − E_{0-0}, which is deduced from the wavelength at 10% maximum absorption intensity for the dye-loaded 3 μm nanocrystalline TiO$_2$ film. As shown in Table 2, the LUMOs

Table 2. Photophysical and Electrochemical Properties of Sensitizers WS-22 and WS-23

dyes	λ_{max}[a] (nm)	ε[a] (M^{-1} cm^{-1})	HOMO[b] (V)	E_{0-0}[c] (V)	LUMO[d] (V)
WS-22	518	22900	0.76	2.01	−1.25
WS-23	545	23600	0.81	1.87	−1.06
	462	34300			

[a]Absorption parameters were obtained in CH$_2$Cl$_2$. [b]HOMO was obtained in CH$_2$Cl$_2$ with ferrocene (0.63 V vs NHE) as the external reference. [c]E_{0-0} was derived from the absorption spectrum on 3 μm nanocrystalline TiO$_2$ film. [d]LUMO was calculated according to LUMO = HOMO − E_{0-0}.

for **WS-22** and **WS-23** are −1.06 and −1.25 V, respectively. That is, the electron injection driving force for both of the dyes is more than 550 mV, which is sufficiently enough for efficient electron injection to the conduction band (E_{cb}) of TiO$_2$ (−0.5 V vs NHE).[3] Moreover, the BDT unit has a higher effect on the LUMO orbital than the HOMO orbital (Table 2).

The absorption property, including light-harvesting efficiency and the absorption coverage, is a key factor that influences the photocurrent. Actually, in recent decades, many researchers have been dedicated to optimizing the photophysical property of sensitizers.[28−33] Figure 4 depicts the absorption spectra of **WS-22** and **WS-23** in CH$_2$Cl$_2$, and the corresponding spectroscopic parameters are summarized in Table 2. **WS-22** exhibits a broad band in the visible region of 400−600 nm corresponding to the intramolecular charge transfer (ICT) from the indoline donor to the cyanoacetic acid acceptor. By introducing BDT as an additional acceptor into **WS-22** to construct the D−A−π−A configuration **WS-23**, the maximum absorption peak exhibits a significant bathochromic shift from 518 to 545 nm along with an obvious increment in molar extinction coefficient. Besides, an additional absorption peak appears at 451 nm and broadens the spectrum in the visible region, which indicates that the incorporation of the BTD moiety in **WS-23** is beneficial to the optimization of the light-harvesting ability.
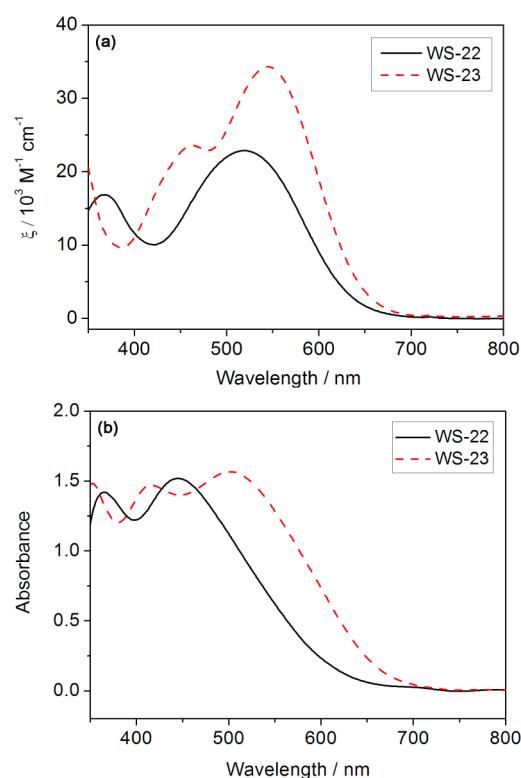
Figure 4. Absorption spectra of **WS-22** and **WS-23** in CH_2Cl_2 (a) and coated on 3 μm transparent TiO_2 film (b).

DFT and TD-DFT are powerful tools for first-principle modeling of ground-state and excited-state properties, respectively. We here employ DFT and TD-DFT calculations to find out the origination of the absorption properties (Table 3). As shown in Table 4, the HOMO orbital of **WS-22** is
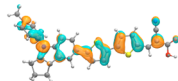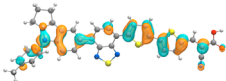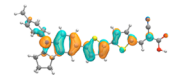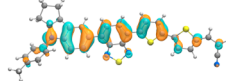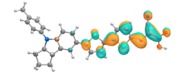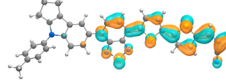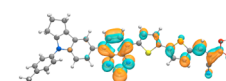
Table 3. Computed Excitation Energies, Oscillator Strengths, and Molecular Orbital Compositions of Excitations with Absorption Wavelengths Longer than 400 nm for WS-22 and WS-23[a]

compounds	excited state	excitation energy	oscillator strength	composition
WS-22	S1	2.61 eV (475 nm)	1.6365	H → L (78%)
				H-1 → L (14%)
WS-23	S1	2.41 eV (515 nm)	1.8531	H-0 → L (72%)
				H-1 → L (12%)
	S2	2.97 eV (417 nm)	0.1473	H → L+1 (60%)
				H-1 → L (24%)

[a]H = HOMO, L = LUMO, H-1 = HOMO - 1, L+1 = LUMO + 1.

mainly located at the donor and π-linker segments, while the LUMO is delocalized over the π-linker and anchoring group. Comparatively, the HOMO for **WS-23** is delocalized over the "D−A−π" segment, while the LUMO is delocalized over the "A−π−A" segment, with prominent overlap on the auxiliary acceptor and π-linker. As indicated, the incorporation of the BTD moiety is favorable to the efficient electron delocalization throughout the whole molecule. According to the calculated result of TD-DFT, the new absorption band located at 400−

Table 4. Contour Plots of Frontier Molecular Orbitals

Compounds	WS-22	WS-23
HOMO-1	-6.44 eV	-6.15 eV
HOMO	-5.53 eV	-5.52 eV
LUMO	-2.88 eV	-3.05 eV
LUMO+1		-2.54 eV

500 nm mainly arose by the intramolecular electron transition of HOMO → LUMO + 1 and HOMO − 1 → LUMO with the contribution of 60% and 24%, respectively (Table 3). On the basis of the contour plots of the aforementioned frontier molecular orbitals shown in Table 4, both of the two-electron transition processes correspond to the transition from the electron donor to the anchoring group, which is beneficial to the efficient electron injection spatially.

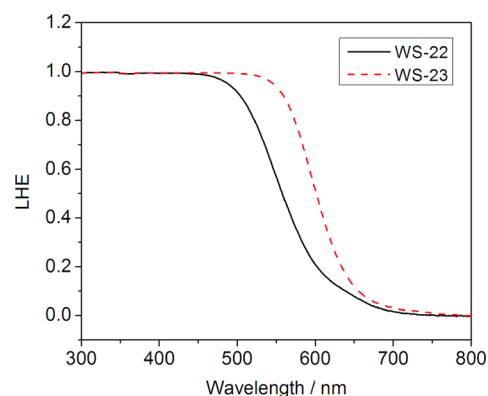Figure 5 shows the LHE spectra of two dyes that are calculated from the absorption spectra of dye-loaded 12 μm

Figure 5. LHE spectra of **WS-22** and **WS-23** calculated from the absorption spectra of dye-loaded 12 μm TiO_2 film.

TiO_2 film through the relation of LHE = $1-10^{-\alpha}$, where α is the intensity of light absorption. The integral area for **WS-23** is 15.6% larger than that for **WS-22** with a calculated wavelength from 300 nm to absorption onset. Obviously, **WS-23** possesses much better LHE performance than that for **WS-22**, including a plateau of 350−600 nm with a value more than 90%. That is, the better light-harvesting ability of **WS-23** is one of the main reasons of its relatively higher J_{sc}.

Effect on V_{oc}. Generally, extending the π-spacer of organic sensitizers always decreases the V_{oc} of DSSCs.[34] However, the device based on **WS-23** shows a higher V_{oc} than that of **WS-22**, differing only with or without the additional electron-withdrawing moiety BTD. As is well known, V_{oc} is determined by the difference between the quasi-Fermi level of TiO_2 (E_{Fn})

1030

dx.doi.org/10.1021/sc500035j | ACS Sustainable Chem. Eng. 2014, 2, 1026−1034

and Fermi level of the redox couple in the electrolyte. As shown in eq 2,[35] E_{Fn} is associated with the conduction band of TiO$_2$ and free electron density in the TiO$_2$ film.

$$V_{oc} = \frac{E_{Fn}}{q} - \frac{E_{redox}}{q} = \frac{E_{CB}}{q} + \frac{kT}{q} \ln\left(\frac{n}{N_{CB}}\right) - \frac{E_{redox}}{q}$$

(2)

where k and q are constant, representing the thermal energy and unit charge, respectively; T is the absolute temperature; n and N_{CB} are the free charge density and acceptable charge density in the conduction band of the TiO$_2$ electrode, respectively.

Considering that the redox couple fabricated in the cells is identical, the difference in V_{oc} here is mainly ascribed to the quasi-Fermi level (E_{Fn}) of the mesoporous TiO$_2$ film. Again, the T and N_{CB} is almost the same for the two series of devices, that is, the V_{oc} is mainly influenced by the conduction band (E_{CB}) and free charge density of TiO$_2$ film (n).

Figure 6 displays the electron density at open circuit as a function of V_{oc} for DSSCs with **WS-22** and **WS-23** to study the
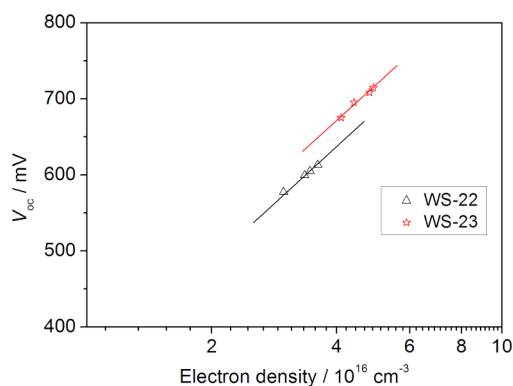
Figure 6. Charge density at open circuit as a function of V_{oc} for DSSCs based on **WS-22** and **WS-23**.

E_{CB} through a stepped light-induced transient (SLIT) measurement. For both dyes, the V_{oc} increases linearly with the logarithm of the electron density, exhibiting a similar slope. Under the given electron density, the V_{oc} of **WS-23** is about 32 mV higher than that of **WS-22**, indicating that the position of the conduction band edge of the DSSCs based on **WS-23** is higher than that of **WS-22**. That is, incorporating an electron-withdrawing group into a D−π−A sensitizer can upshift the conduction band edge of mesoporous semiconductor, which is beneficial to output a higher photovoltage.

Theoretically, E_{CB} is dependent on the dipole moment of anchored sensitizers according to eq 3.[36] Here, q is the unit charge, and ε_0 and ε are the vacuum permittivity and the dielectric constant of the organic monolayer, respectively. γ is the dye concentration at surface, and μ_{normal} is the vertical dipole moment of individual dye molecule. Obviously, sensitizers with large μ_{normal} can upshift the E_{CB} efficiently.

$$\Delta E_{CB} = -\frac{q\mu_{normal}\gamma}{\varepsilon_0\varepsilon}$$

(3)

To gain further insight into the difference of the V_{oc} originated from the conduction band, the dipole moments of **WS-22** and **WS-23** at their optimized geometry were calculated by the hybrid density functional theory (B3LYP) with the 6-31G* basis set as implemented in the Gaussian 03 program.

Considering their bidentate binding mode, the C2 axis was set parallel to the x-axis, and the TiO$_2$ surface plane was parallel to the y−z plane. The μ_{normal} of the sensitizers can be estimated through the dipole moment along the x-axis. As shown in Figure 7, the vertical component of dipoles (x components) of
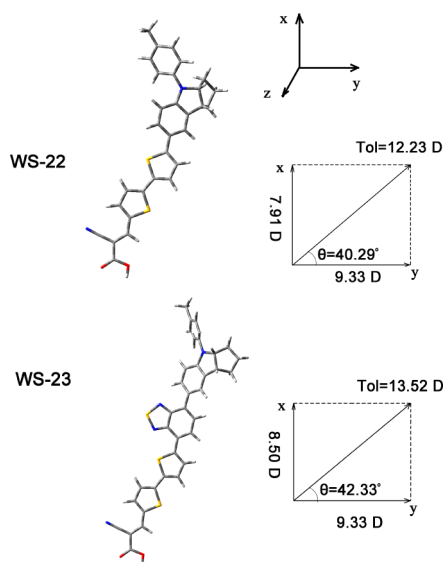
Figure 7. Optimized geometrical structures and calculated total dipole moments of **WS-22** and **WS-23**.

two sensitizers possess the same direction but with different magnitude (7.91 and 8.50 D for **WS-22** and **WS-23**, respectively). Once adsorbed on TiO$_2$, the larger dipole moment along the direction for **WS-23** can lead to more negative charges located closer to the TiO$_2$ surface than that of **WS-22**, resulting in a larger CB energy level upshift.[11,37]

As discussed above, besides μ_{normal}, the free electron density in the TiO$_2$ electrode is another important parameter that influences open circuit photovoltage, which is associated with the balance of the electron injection and charge recombination process and can be evaluated through an electron lifetime. Accordingly, the SLIT and EIS measurements were carried out to picture the relationship of V_{oc} and electron lifetime as a function of electron density.[30,38]

Figure 8 shows the electron lifetime as a function of charge density at the open circuit for the DSSCs based on **WS-22** and **WS-23**. The charge recombination lifetime decreases with charge density and follows a power law relation with the same
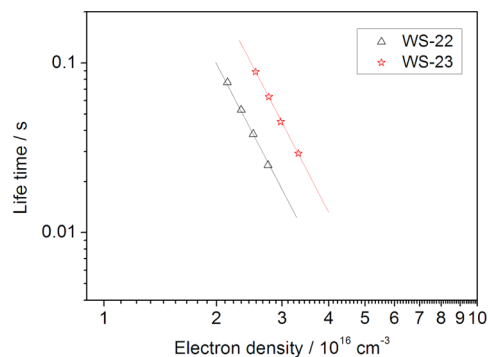
Figure 8. Charge recombination lifetime as a function of charge density for DSSCs based on **WS-22** and **WS-23**.

slope, indicative of the same recombination mechanism. At a fixed electron density, the electron lifetime for the DSSC based on **WS-23** is about 2.55-fold with respect to that of **WS-22**. It is indicative that **WS-23** is more effective than **WS-22** in blocking I_3^- ions approaching the TiO_2 surface for charge recombination, thus showing an improvement in V_{oc}.[39] Considering that the optimization from **WS-22** to **WS-23** is 57 mV, while the conduction band uplift for **WS-23**-based solar cells is only about 23 mV, it can be assumed that the contribution of the retarding charge recombination of **WS-23** in V_{oc} is about 34 mV. Thus, the improvement of V_{oc} in **WS-23** is originated by a synergy contribution of the uplifting of E_{CB} and inhibition of charge recombination.

To further gain insight into the internal reason for the different electron lifetimes of the two DSSCs, we conducted an impedance (EIS) analysis, an important method to study the charge transfer resistance of the TiO_2 dye−electrolyte interface.[40] Figure 9 shows the charge transfer resistance of the
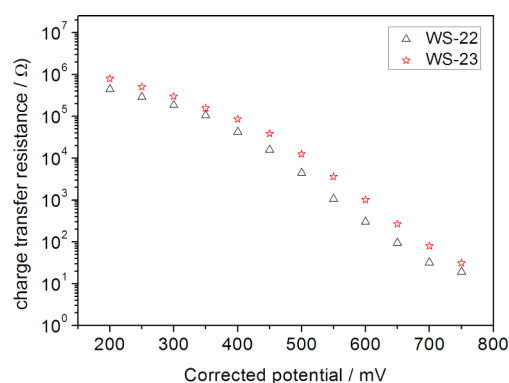

Figure 9. Charge transfer resistance of the DSSCs based on **WS-22** and **WS-23** at the different potentials.

DSSCs based on **WS-22** and **WS-23** with 15 mM DCA at the different potential. As shown in Figure 9, the **WS-23**-based DSSCs exhibited higher charge transfer resistance with respect to **WS-22** under the same potential. With the applied bias potential set at 600 and 700 mV, the charge resistances for **WS-23** were 3.39- and 2.49-fold of those for **WS-22**, further confirming that **WS-23**-sensitized solar cells exhibit longer electron lifetime. Apparently, the incorporation of an auxiliary acceptor BTD is favorable to the optimization of the charge recombination process.

Effect on Dye Stability. Device stability is crucial for the practical application of DSSCs along with high efficiency. Generally, the long-term test of device stability is always studied with fabricating solar cells based on a stable ionic liquid electrolyte. The method needs continuous irradiation under AM 1.5 light for a long time. Katoh and co-workers reported a quick and convenient method to evaluate the stability of the sensitizers just by irradiating the dye adsorbed on TiO_2 films without a redox electrolyte.[41] Figure 10 shows the absorption curves of dyes **WS-22** and **WS-23** with aging upon light irradiation of AM 1.5 light (5 or 30 min). After light irradiation, the absorbance of **WS-22** at 400−600 nm decreased, suggesting that it is not stable during its cation state lifetime. However, by introducing an additional electron-withdrawing moiety BTD to the π-spacer, the absorbance of **WS-23** almost keeps the same before and after light irradiation compared to **WS-22**, indicating that the D−A−π−A configuration can indeed improve stability.
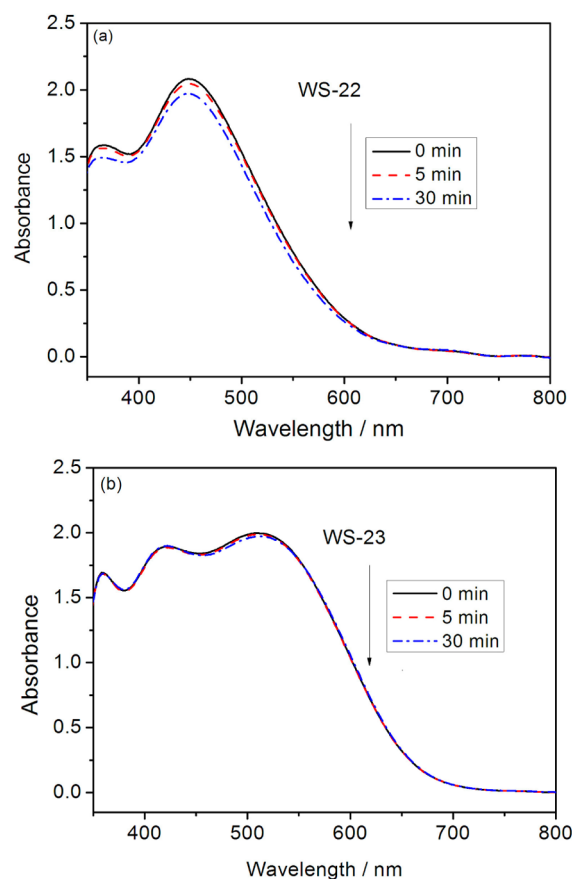

Figure 10. Absorption spectra of **WS-22** (a) and **WS-23** (b) adsorbed on nanocrystalline TiO_2 films before (black line) and after light irradiation for 5 min (red line) and 30 min (blue line).

CONCLUSIONS

We have synthesized two organic sensitizers with or without the BTD moiety as an auxiliary acceptor to systematically investigate the advantages of the D−A−π−A configuration sensitizer. By introducing BDT into organic D−π−A dyes, **WS-23** achieved an optimizing efficiency (η = 8.15%), with an improvement of 37.5% in comparison to **WS-22**. With respect to **WS-22**, the absorption spectrum and electron transition process for **WS-23** is more complicated, with an additional absorption peak in the region of 400−500 nm. SLIT measurements and dipole moment calculations indicate that the incorporation of an auxiliary acceptor BTD can efficiently upshift the conduction band of the TiO_2 film, resulting in a larger photovoltage. EIS measurements further point out that the charge recombination process with I_3^- is retarded in **WS-23**-based solar cells. These results indicate that the D−A−π−A-featured sensitizer is an emerging candidate for efficient dye-sensitized solar cells.

AUTHOR INFORMATION

Corresponding Author
*Fax: (+86) 21-6425-2758. E-mail: whzhu@ecust.edu.cn.
Notes
The authors declare no competing financial interest.

ACKNOWLEDGMENTS

1032

dx.doi.org/10.1021/sc500035j | ACS Sustainable Chem. Eng. 2014, 2, 1026−1034

■ REFERENCES

(1) O'Regan, B.; Grätzel, M. A low-cost, high-efficiency solar cell based on dye-sensitized colloidal TiO$_2$ films. *Nature* **1991**, *353*, 737−740.

(2) Zhang, S. F.; Yang, X. D.; Numata, Y.; Han, L. Y. Highly efficient dye-sensitized solar cells: progress and future challenges. *Energy Environ. Sci.* **2013**, *6*, 1443−1464.

(3) Hagfeldt, A.; Boschloo, G.; Sun, L. C.; Kloo, L.; Pettersson, H. Dye-sensitized solar cells. *Chem. Rev.* **2010**, *110*, 6595−6663.

(4) Mishra, A.; Fischer, M. K.; Bäuerle, P. Metal-free organic dyes for dye-sensitized solar cells: From structure−property relationships to design rules. *Angew. Chem., Int. Ed.* **2009**, *48*, 2474−2499.

(5) Liang, M.; Chen, J. Arylamine organic dyes for dye-sensitized solar cells. *Chem. Soc. Rev.* **2013**, *42*, 3453−3488.

(6) Cai, N.; Zhang, J.; Xu, M. F.; Zhang, M.; Wang, P. Improving the photovoltage of dithienopyrrole dye-sensitized solar cells via attaching the bulky bis(octyloxy)biphenyl moiety to the conjugated π-linker. *Adv. Funct. Mater.* **2013**, *23*, 3539−3547.

(7) Wan, Z. Q.; Jia, C. Y.; Duan, Y. D.; Chen, X. M.; Lin, Y.; Shi, Y. Novel organic dye employing dithiafulvenyl-substituted arylamine hybrid donor unit for dye-sensitized solar cells. *Org. Electron.* **2013**, *14*, 2132−2138.

(8) Ren, X. M.; Jiang, S. H.; Cha, M. Y.; Zhou, G.; Wang, Z.-S. Thiophene-bridged double D-π-A dye for efficient dye-sensitized solar cell. *Chem. Mater.* **2012**, *24*, 3493−3499.

(9) Shen, P.; Liu, Y. J.; Huang, X. W.; Zhao, B.; Xiang, N.; Fei, J. J.; Liu, L. M.; Wang, X. Y.; Huang, H.; Tan, S. T. Efficient triphenylamine dyes for solar cells: Effects of alkyl-substituents and π-conjugated thiophene unit. *Dyes Pigm.* **2009**, *83*, 187−197.

(10) Shen, P.; Liu, X. P.; Jiang, S. H.; Huang, Y. S.; Yi, L.; Zhao, B.; Tan, S. T. Effects of aromatic π-conjugated bridges on optical and photovoltaic properties of *N,N*-diphenylhydrazone-based metal-free organic dyes. *Org. Electron.* **2011**, *12*, 1992−2002.

(11) Chai, Q. P.; Li, W. Q.; Zhu, S. Q.; Zhu, S. Q.; Zhang, Q.; Zhu, W. H. Influence of donor configurations on photophysical, electrochemical and photovoltaic performances in D-π-A organic sensitizers. *ACS Sustainable Chem. Eng.* **2013**, *2*, 239−247.

(12) Li, W. Q.; Wu, Y. Z.; Li, X.; Xie, Y. S.; Zhu, W. H. Absorption and photovoltaic properties of organic solar cell sensitizers containing fluorene unit as conjunction bridge. *Energy Environ. Sci.* **2011**, *4*, 1830−1837.

(13) Zhu, W. H.; Wu, Y. Z.; Wang, S. T.; Li, W. Q.; Li, X.; Chen, J.; Wang, Z.-S.; Tian, H. Organic D-A-π-A solar cell sensitizers with improved stability and spectral response. *Adv. Funct. Mater.* **2011**, *21*, 756−763.

(14) Cui, Y.; Wu, Y. Z.; Lu, X. F.; Zhang, X.; Zhou, G.; Miapeh, F. B.; Zhu, W. H; Wang, Z.-S. Incorporating benzotriazole moiety to construct D-A-π-A organic sensitizers for solar cells: Significant enhancement of open-circuit photovoltage with long alkyl group. *Chem. Mater.* **2011**, *23*, 4394−4401.

(15) Pei, K.; Wu, Y. Z.; Wu, W. J.; Zhang, Q.; Chen, B.; Tian, H.; Zhu, W. H. Constructing organic D-A-π-A-featured sensitizers with a quinoxaline unit for high-efficiency solar cells: The effect of an auxiliary acceptor on the absorption and the energy level alignment. *Chem.—Eur. J.* **2012**, *18*, 8190−8200.

(16) Wu, Y. Z.; Zhu, W. H. Organic sensitizers from D-π-A to D-A-π-A: effect of the internal electron-withdrawing units on molecular absorption, energy levels and photovoltaic performances. *Chem. Soc. Rev.* **2013**, *42*, 2039−2058.

(17) Guo, X. G.; Zhou, N. J.; Lou, S. J.; Hennek, J. W.; Ponce Ortiz, R.; Butler, M. R.; Boudreault, P. L.; Strzalka, J.; Morin, P. O.; Leclerc, M.; Lopez Navarrete, J. T.; Ratner, M. A.; Chen, L. X.; Chang, R. P.; Facchetti, A.; Marks, T. J. Bithiopheneimide-dithienosilole/dithienogermole copolymers for efficient solar cells: Information from structure-property-device performance correlations and comparison to thieno[3,4-*c*]pyrrole-4,6-dione analogues. *J. Am. Chem. Soc.* **2012**, *134*, 18427−18439.

(18) Shi, J.; Chen, J. N.; Chai, Z. F.; Wang, H.; Tang, R. L.; Fan, K.; Wu, M.; Han, H. W.; Qin, J. G.; Peng, T. Y.; Li, Q. Q.; Li, Z. High performance organic sensitizers based on 11,12-bis(hexyloxy) dibenzo-[*a,c*]phenazine for dye-sensitized solar cells. *J. Mater. Chem.* **2012**, *22*, 18830−18838.

(19) Wang, L.; Shen, P.; Cao, Z. C.; Liu, X. P.; Huang, Y. S.; Liu, C. Y.; Chen, P.; Zhao, B.; Tan, S. T. Effects of the acceptors in triphenylamine-based D-A'-π-A dyes on photophysical, electrochemical, and photovoltaic properties. *J. Power Sources* **2014**, *246*, 831−839.

(20) Ying, W. J.; Yang, J. B.; Wielopolski, M.; Moehl, T.; Moser, J.-E.; Comte, P.; Hua, J. L.; Zakeeruddin, S. M.; Tian, H.; Grätzel, M. New pyrido[3,4-*b*]pyrazine-based sensitizers for efficient and stable dye-sensitized solar cells. *Chem. Sci.* **2014**, *5*, 206−214.

(21) Yum, J.-H.; Holcombe, T. W.; Kim, Y.; Yoon, J.; Rakstys, K.; Nazeeruddin, M. K.; Grätzel, M. Towards high-performance DPP-based sensitizers for DSC applications. *Chem. Commun.* **2012**, *48*, 10727−10729.

(22) Liu, Y. S.; Wan, X. J.; Wang, F.; Zhou, J. Y.; Long, G. K.; Tian, J. G.; Chen, Y. S. High-performance solar cells using a solution-processed small molecule containing benzodithiophene unit. *Adv. Mater.* **2011**, *23*, 5387−5391.

(23) Perdew, J. P.; Burke, K.; Ernzerhof, M. Generalized gradient approximation made simple. *Phys. Rev. Lett.* **1996**, *77*, 3865−3868.

(24) Adamo, C.; Barone, V. Toward reliable density functional methods without adjustable parameters: The PBE0 model. *J. Chem. Phys.* **1999**, *110*, 6158−6170.

(25) McLean, A. D.; Chandler, G. S. Contracted Gaussian basis sets for molecular calculations. I. Second row atoms, Z=11−18. *J. Chem. Phys.* **1980**, *72*, 5639−5648.

(26) Krishnan, R.; Binkley, J. S.; Seeger, R.; Pople, J. A. Self-consistent molecular orbital methods. XX. A basis set for correlated wave functions. *J. Chem. Phys.* **1980**, *72*, 650−654.

(27) Yanai, T.; Tew, D. P.; Handy, N. C. A new hybrid exchange−correlation functional using the Coulomb-attenuating method (CAM-B3LYP). *Chem. Phys. Lett.* **2004**, *393*, 51−57.

(28) Tomasi, J.; Mennucci, B.; Cammi, R. Quantum mechanical continuum solvation models. *Chem. Rev.* **2005**, *105*, 2999−3094.

(29) Ito, S.; Murakami, T. N.; Comte, P.; Liska, P.; Grätzel, C.; Nazeeruddin, M. K.; Grätzel, M. Fabrication of thin film dye sensitized solar cells with solar to electric power conversion efficiency over 10%. *Thin Solid Films* **2008**, *516*, 4613−4619.

(30) Nakade, S.; Kanzaki, T.; Wada, Y.; Yanagida, S. Stepped light-induced transient measurements of photocurrent and voltage in dye-sensitized solar cells: application for highly viscous electrolyte systems. *Langmuir* **2005**, *21*, 10803−10807.

(31) Zhu, X. Z.; Tsuji, H.; Yella, A.; Chauvin, A.-S.; Grätzel, M.; Nakamura, E. New sensitizers for dye-sensitized solar cells featuring a carbon-bridged phenylenevinylene. *Chem. Commun.* **2013**, *49*, 582−584.

(32) Zhang, J.; Yao, Z. Y.; Cai, Y. C.; Yang, L.; Xu, M. F.; Li, R. Z.; Zhang, M.; Dong, X. D.; Wang, P. Conjugated linker correlated energetics and kinetics in dithienopyrrole dye-sensitized solar cells. *Energy Environ. Sci.* **2013**, *6*, 1604−1614.

(33) Xu, X.; Wang, H.; Gong, F.; Zhou, G.; Wang, Z.-S. Performance enhancement of dye-sensitized solar cells using an ester-functionalized imidazolium iodide as the solid state electrolyte. *ACS Appl. Mater. Interfaces* **2013**, *5*, 3219−3223.

(34) Liu, J. Y.; Li, R. Z.; Si, X. Y.; Zhou, D. F.; Shi, Y. S.; Wang, Y. H.; Jing, X. Y.; Wang, P. Oligothiophene dye-sensitized solar cells. *Energy Environ. Sci.* **2010**, *3*, 1924−1928.

(35) Marinado, T.; Nonomura, K.; Nissfolk, J.; Karlsson, M. K.; Hagberg, D. P.; Sun, L. C.; Mori, S.; Hagfeldt, A. How the nature of triphenylamine-polyene dyes in dye-sensitized solar cells affects the open-circuit voltage and electron lifetimes. *Langmuir* **2010**, *26*, 2592−2598.

(36) Krüger, J.; Bach, U.; Grätzel, M. Modification of TiO_2 heterojunctions with benzoic acid derivatives in hybrid molecular solid-state devices. *Adv. Mater.* **2000**, *12*, 447−451.

(37) Chen, P.; Yum, J. H.; Angelis, F. D.; Mosconi, E.; Fantacci, S.; Moon, S.-J.; Baker, R. H.; Ko, J.; Nazeeruddin, M. K.; Grätzel, M. High open-circuit voltage solid-state dye-sensitized solar cells with organic dye. *Nano Lett.* **2009**, *9*, 2487−2492.

(38) Ondersma, J. W.; Hamann, T. W. Impedance investigation of dye-sensitized solar cells employing outer-sphere redox shuttles. *J. Phys. Chem. C* **2010**, *114*, 638−645.

(39) Qu, S. Y.; Qin, C. J.; Islam, A.; Wu, Y. Z.; Zhu, W. H.; Hua, J. L.; Tian, H.; Han, L. Y. A novel D-A-π-A organic sensitizer containing a diketopyrrolopyrrole unit with a branched alkyl chain for highly efficient and stable dye-sensitized solar cells. *Chem. Commun.* **2012**, *48*, 6972−6974.

(40) Yang, X. D.; Yanagida, M.; Han, L. Y. Reliable evaluation of dye-sensitized solar cells. *Energy Environ. Sci.* **2013**, *6*, 54−66.

(41) Katoh, R.; Furube, A.; Mori, S.; Miyashita, M.; Sunahara, K.; Koumura, N.; Hara, K. Highly stable sensitizer dyes for dye-sensitized solar cells: role of the oligothiophene moiety. *Energy Environ. Sci.* **2009**, *2*, 542−546.